A computational model of the ribbon synapse

Michael A. Sikora [*,1], Jon Gottesman [1], Robert F. Miller

Department of Neuroscience, University of Minnesota, 6-146 Jackson Hall, 321 Church St SE, Minneapolis, MN 55455, USA

Abstract

A model of the ribbon synapse was developed to replicate both pre- and postsynaptic functions of this glutamatergic juncture. The presynaptic portion of the model is rich in anatomical and physiological detail and includes multiple release sites for each ribbon based on anatomical studies of presynaptic terminals, presynaptic voltage at the terminal, the activation of voltage-gated calcium channels and a calcium-dependent release mechanism whose rate varies as a function of the calcium concentration that is monitored at two different sites which control both an ultrafast, docked pool of vesicles and a release ready pool of tethered vesicles. The postsynaptic portion of the program models diffusion of glutamate and the physiological properties of glutamatergic neurotransmission in target cells. We demonstrate the behavior of the model using the retinal bipolar cell to ganglion cell ribbon synapse. The model was constrained by the anatomy of salamander bipolar terminals based on the ultrastructure of these synapses and presynaptic contacts were placed onto realistic ganglion cell morphology activated by a range of ribbon synapses (46–138). These inputs could excite the cell in a manner consistent with physiological observations. This model is a comprehensive, first-generation attempt to assemble our present understanding of the ribbon synapse into a domain that permits testing our understanding of this important structure. We believe that with minor modifications of this model, it can be fine tuned for other ribbon synapses.
© 2004 Elsevier B.V. All rights reserved.

Keywords: Ribbon synapse; Exocytotic mechanism; Ultrafast pool; Release site vesicle pool

The ribbon synapse is a specialized connection between nerve cells characterized by the presence of a unique presynaptic structure that has been termed the synaptic ribbon or dense body. This structure has been found in the presynaptic terminals of rods, cones and bipolar cells of the vertebrate retina (Dowling and Boycott, 1966; Kidd, 1962; Sjöstrand, 1953, 1958), hair cells of the cochlea and vestibular organ (Smith and Sjöstrand, 1961; Wersall et al., 1965), the electroreceptors and lateral line receptors of fish (Hama, 1965; Wachtel and Szamier, 1966), pinealocytes (Vollrath and Huss, 1973) and several invertebrate neuromuscular junctions (Katz et al., 1993; Kosaka and Ikeda, 1983).

While the precise dimensions of the ribbon vary both within a cell type within a species as well as across cell types, all ribbons share the fact that synaptic vesicles are tethered to the surface of the ribbon. This has led to the common interpretation that the ribbon is a specialization for exocytosis in these cells. In support of this idea is the finding that the number of vesicles tethered to the dense body of hair cells is reduced following a depolarizing stimulus that causes release of vesicles (Lenzi et al., 2002). Another interesting commonality for the cell types possessing ribbons is that these cells signal changes to the postsynaptic cell via graded potentials and not action potentials. Also, many of the presynaptic proteins related to vesicular fusion at the ribbon have been identified. While many of these proteins are shared with those found at classic CNS active zones, there are some proteins that are unique to ribbon synapses (see Lenzi and von Gersdorff, 2001; Morgans, 2000 for reviews).

The photoreceptors and bipolar cells of the vertebrate retina secrete glutamate as their neurotransmitter. Like other secretory synapses, glutamate in these cells is packaged into single vesicles that are released into the extracellular space in a calcium-dependent manner. Where conventional synapses

---

usually have dozens of vesicles in the presynaptic terminal, bipolar and photoreceptor terminals are associated with thousands of vesicles. Indeed, the giant bipolar terminal of the goldfish has as many as 1 million vesicles distributed within a space that contains 10–100 ribbons (von Gersdorff et al., 1996).

Studies of ribbon synapses using cell capacitance measurements to determine the rate of exocytosis suggest that high rates of vesicular fusion can be achieved through this specialized synaptic structure. Rates of thousands of vesicles/s have been reported for synaptic terminals with this experimental approach. These high rates of vesicular release are important to appreciate the function of photoreceptors and bipolar cells, since they generate sustained, analog responses to light stimulation and maintain neurotransmitter release at some level throughout the life of the animal.

We have generated a detailed model of a ribbon synapse that includes the presynaptic and postsynaptic events and used that model to place multiple synapses on the realistic morphology of a retinal ganglion cell. The model parameters reported in this study conform to physiological analysis of miniature postsynaptic excitatory currents and ultrastructural studies on ribbon synapses in the salamander retina. Our results suggest that a single ribbon synapse in this species supports a graded rate of vesicular release with a maximum of about 600 vesicles/s. Using ribbon synapses with this configuration, we find that a relatively small number are required to provide robust support of postsynaptic currents sufficient to
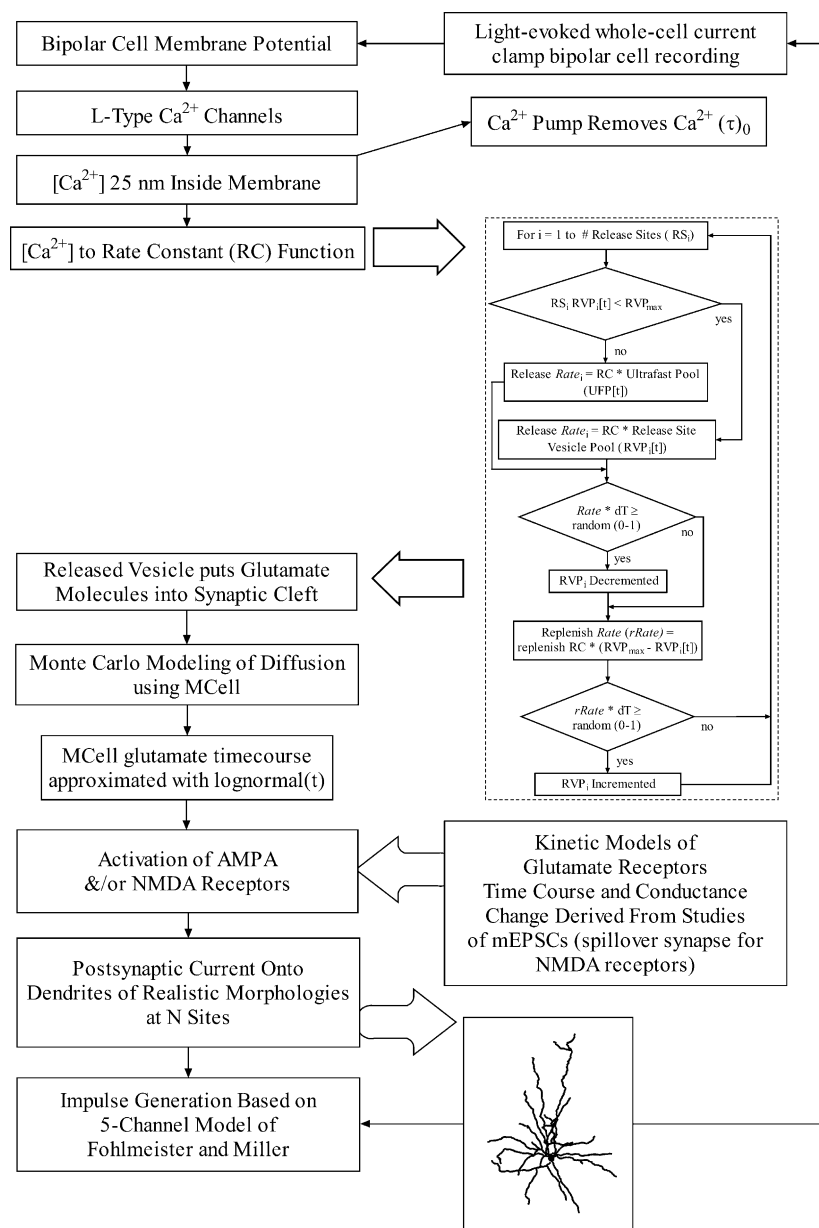

Fig. 1. A flow diagram of the program elements in the ribbon synapse model.

generate impulse activity in a manner consistent with physiological observations.

We have designed the implementation presented here be easily extended to other systems so that the anatomical and physiological differences between ribbon synapses in cells other than the retinal bipolar cell can be modeled.

1. Methods

1.1. Model overview

Programming of the main simulation model was done in NEURON (Hines and Carnevale, 1997, 2001) and the code is available through the ModelDB website (http://senselab.med.yale.edu/senselab/modeldb). Diffusion modeling was performed using MCell and visualized using DReAMM (http://www.mcell.psc.edu). A flow diagram of the program components and logic is shown in Fig. 1. The variable names used in the program are shown in the accompanying Table 1 and each mechanism will be described below.

1.2. Anatomical parameters

Analysis of the ultrastructure of salamander bipolar cell ribbon synapses was performed on serial electron micrographs of nine ribbon synapses like the example shown in Fig. 2A. These data allowed determination of the size of synaptic vesicles (mean diameter = 26.4 nm ± 0.17 S.E.) and the length and height of the ribbon (125–150 nm) (Miller et al., 2001a,b). There are typically 16–25 tethered vesicles on one side of the ribbon and Fig. 2C shows the case of five rows of vesicles in five columns. Thus, there are 10 release sites per ribbon with fusion occurring for vesicles on either side of the ribbon.

Fig. 2B and C shows a model dyad synapse between a tiger salamander bipolar cell process containing a presynap-

tic ribbon and two postsynaptic processes each expressing AMPA receptors on their surface. Fig. 2B provides a cross-section view of the synapse including a vesicle undergoing exocytosis and release of glutamate into the synaptic cleft. An oblique view is displayed in Fig. 2C which is used to highlight the fact that vesicle fusion is believed to occur along the entire length of the ribbon structure. The fusion sites will be referred to as release sites for each ribbon and the entire ribbon will be considered the active zone of the dyad synapse.

Our use of multiple release sites reflects the ultrastructural data showing vesicles in close apposition to the presynaptic membrane along the length of the ribbon as well as the clustering of calcium channels at ribbons (Lenzi et al., 1999; Miller et al., 2001a,b; Nachman-Clewner et al., 1999; Roberts et al., 1990; von Gersdorff et al., 1996). From a computational standpoint, it needs to be noted that all of the behavior reported here for our model could be replicated using different algorithms that would be applied to a single release site.

The computational model of the ribbon allows for specification of the size of the tethered vesicle pool and the number of release sites per ribbon. For example, we made use of ultrastructural data for the goldfish giant bipolar terminal (von Gersdorff et al., 1996), which differs from the salamander, when modeling exocytosis in this species (Figs. 4, 7 and 8).

1.3. Exocytotic mechanism – presynaptic calcium concentration

The first step in the simulation is the control of the bipolar cell membrane potential which drives the conductance of an L-type calcium channel whose *I–V* properties are shown in Fig. 3A. We only modeled L channels as they are solely responsible for the calcium influx that drives vesicular release in both salamander and goldfish bipolar cells (Heidelberger and Matthews, 1992; Maguire et al., 1989), but other calcium channel types could easily be implemented. The maximum

Table 1
The variables used in the ribbon synapse model as diagramed in the flow chart of Fig. 1

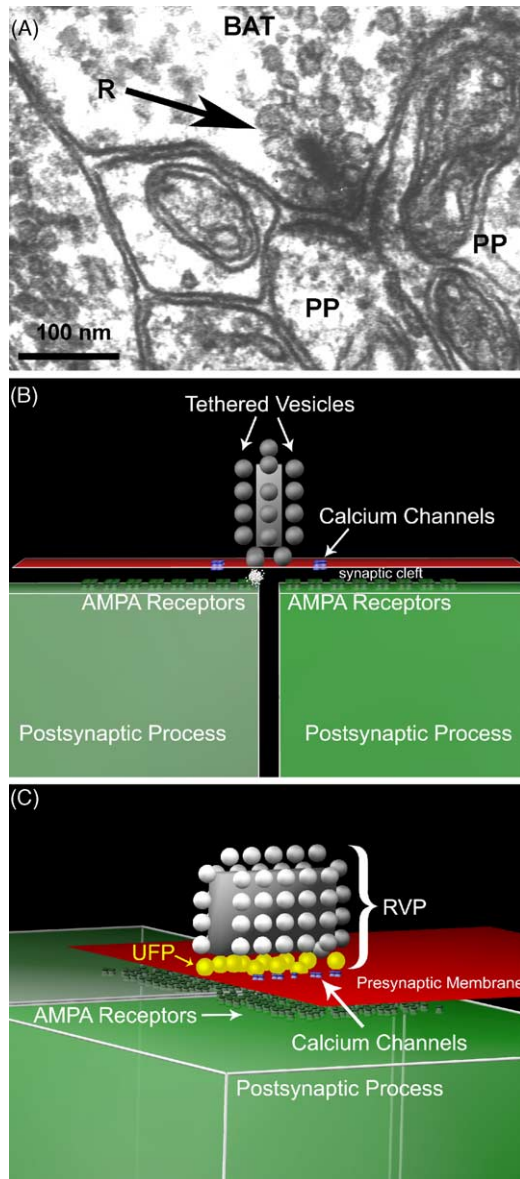| Variable name	Variable definition	Variable units
RS	Number of release sites per ribbon	Release sites
UFP	Number of docked vesicles at ribbon	Number of vesicles
RVP	Number of vesicles tethered above release site	Number of vesicles
RVP_{max}	Maximum size of the RVP	Number of vesicles
d_1	Distance of Ca^{2+} sensor used by docked vesicles (UFP)	nm
d_2	Distance of Ca^{2+} sensor used by non-docked, tethered vesicles	nm
τ_{d_1}	Time constant for removal of Ca^{2+} at d_1	s
τ_{d_2}	Time constant for removal of Ca^{2+} at d_2	s
RC_{d_1}	Rate constant of exocytosis for UFP: depends on $[Ca^{2+}]$ at d_1 (see Fig. 4)	s^{-1}
RC_{d_2}	Rate constant of exocytosis for RVP: depends on $[Ca^{2+}]$ at d_2 (see Fig. 4)	s^{-1}
Rate	Calculated rate of release for a single release site	vesicles/s
rRC	Rate constant for replenishment of the tethered vesicle pool	s^{-1}
rRate	Calculated rate of replenishment	vesicles/s
$AMPA_{gmax}$	Maximum conductance for the AMPA receptor mechanism	nS
$NMDA_{gmax}$	Maximum conductance for the NMDA receptor mechanism	nS

Fig. 2. (A) An electron micrograph of a representative bipolar cell ribbon synapse in the tiger salamander retina. Analysis of serial sections of nine synapses were used to determine the mean vesicle diameter and length and height of the ribbon. BAT – bipolar axon terminal; PP – postsynaptic process; R – ribbon. (B) A rendered image of a simulated dyad ribbon synapse generated by MCell and DReAMM (http://www.mcell.psc.edu/) with a view similar to the EM data in panel (A). A single vesicle is shown fusing at the base of the ribbon and releasing its contents into the synaptic cleft. (C) A rotated view of the dyad to illustrate the fact that there is more than one release site per ribbon (active zone). The vesicles shown in yellow at the base of the ribbon represent those vesicles docked to the presynaptic membrane that constitute the ultrafast pool (UFP). The "column" of vesicles located vertically above each site of vesicle fusion, or release site, is termed the release site vesicle pool (RVP).

conductance density of the channel mechanism is determined by the experimenter and Fig. 3A shows an example with the L channel parameters set to match the typical whole cell current through L-type calcium channels measured in salamander bipolar cells (Maguire et al., 1989; Thoreson, 2000). For
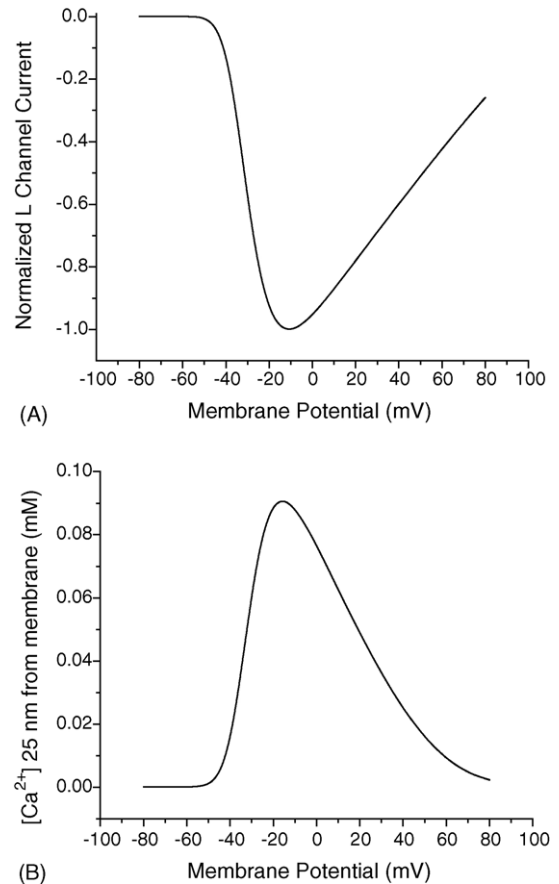

Fig. 3. (A) The normalized current–voltage relationship of salamander presynaptic calcium channels. This L-type channel was modeled using the formulation of Fohlmeister and Miller (1997) with the kinetics (α and β from their Table 1) modified to adjust the maximum activation voltage to match physiological data in the amphibian. A voltage ramp from -80 to $+80$ mV was applied to an isopotential single-compartment structure at a rate of 0.08 mV/ms. The peak current is evoked at -10.8 mV and is half maximal at -31.5 mV. The curve to the right of peak is shallow compared to published examples and is the result of the non-Boltzmann formulation of the model channel. It is of no consequence in the simulations here because applied voltage is never greater than peak. (B) The resultant calcium concentration measured 25 nm from the presynaptic membrane to the same voltage-ramp protocol as in (A). Model parameters: L channel conductance density $= 0.0012$ S/cm^2; $d_1 = 25$ nm; $\tau_{d_1} = 0.8$ s.

simulation of the goldfish giant bipolar terminal, we modified the L channel kinetics to match the *I–V* curve described by von Gersdorff and Matthews (1994).

The calcium concentration which drives exocytosis will be determined by the interplay between the diffusion of calcium entering through the ion channels, the spatial distribution of the channels in the presynaptic membrane relative to the locations of the calcium sensor and the activity of endogenous calcium buffers and/or pumps. Calcium influx is likely to be complex and potentially specific to presynaptic cell types (Roberts, 1994). Calcium buffering may likewise be variable in different cell types based on differences in the nature of both spatially fixed and freely diffusible buffers (Burrone et al., 2002; Roberts, 1994).

In the absence of any available freeze fracture electron microscopic data for the localization of the calcium channels in bipolar cell terminals or data on calcium buffering in salamander bipolar terminals, we have chosen to use a computationally efficient and simplified estimation of calcium concentration near the presynaptic membrane via the following relationship:

$$\frac{d[Ca^{2+}]_d}{dt} = \left(\frac{I_{Ca}}{2 \times F \times d}\right) - \frac{[Ca^{2+}]_d - [Ca^{2+}]_{rest}}{\tau} \qquad (1)$$

where $[Ca^{2+}]_d$ is the calcium concentration at depth $= d$ inside the presynaptic membrane, I_{Ca} the current density through the L channels, F the Faraday constant, $[Ca^{2+}]_{rest}$ the resting level of calcium in the terminal (100 nM for our simulations) and τ the time constant of removal for calcium. The factor of 2 is the valence of the calcium ions.

Calcium influx is calculated from the product of the calcium current across the membrane surface area (I_{Ca}) and the surface to volume ratio of the structure in question. Our interest is in the calcium concentration in volumes very close to the membrane. For distances very near to the membrane the surface to volume ratio is effectively the reciprocal of the depth (d).

Removal of calcium from the cytosol is expressed by the second term in Eq. (1) which occurs with time constant τ. Our method of calcium removal does not act as an extrusion pump and does not directly generate any current in the presynaptic terminal. We chose this oversimplification of calcium homeostasis because of the lack of data on the buffering in the bipolar cells of the tiger salamander and also for computational efficiency. The model could be modified in the future to produce extrusion behavior as shown by Zenisek and Matthews (2000) and the buffering behavior as shown for the goldfish giant bipolar terminal in the experiments of Burrone et al. (2002).

The value of d can be set to correspond to the distance between the calcium channels and the location of the calcium sensor of the vesicular release machinery where this can be approximated. Fig. 3B shows the calcium concentration 25 nm from the membrane in response to the voltage ramp applied to the bipolar cell whose L-type calcium channel produced the I–V plot in the upper panel.

1.4. Exocytotic mechanism – control of release rate by calcium microdomain concentration

The relationship between calcium in the bipolar terminal compartment and the release of vesicles is a critical factor in determining the behavior of the model synapse. As this relationship is different at different synapses (Heidelberger, 2001; Thoreson et al., 2004) the model allows the experimenter to specify the relationship in the form of a function which will be applied to each ribbon. For our simulations of the bipolar cell to ganglion cell excitatory synapse, we relied on the data of Heidelberger et al. (1994) relating flash
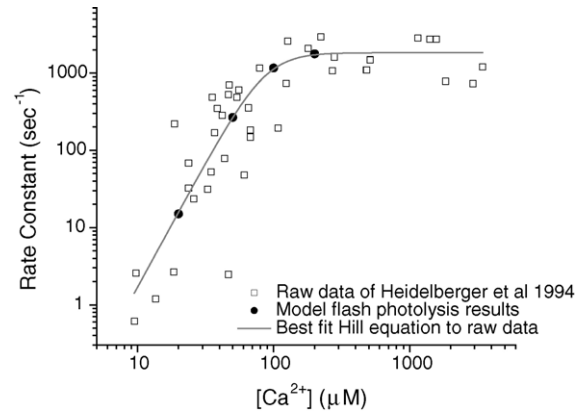

Fig. 4. Rate constant for vesicular release as a function of $[Ca^{2+}]$ redrawn from Heidelberger et al. (1994). The best-fit Hill equation, RC $= V_{max} \times [Ca^{2+}]^n / k^n + [Ca^{2+}]^n$ to these data had the following parameters: $V_{max} = 1842.47$, $k = 86.73$, $n = 3.24$ and is plotted as the solid gray line. Also shown (filled circles) are the rate constants derived from single exponential fits to the simulation data of Fig. 7.

photolysis of caged calcium to exocytosis as measured by capacitance (open squares in Fig. 4). These data were then fit by a Hill equation (solid line, Fig. 4). The best-fitting Hill function was used in the program solely for its computational efficiency and does not reflect any assumptions regarding the underlying mechanism. At each time step of the program, the calcium concentration in the microdomain is obtained and the Hill equation is used to derive the instantaneous rate constant (RC) for vesicular release.

The model next determines exocytotic events at each release site in a simulation. The algorithm keeps track of the number of vesicles that are aligned in a column above each release site which we have termed the release site vesicle pool (RVP, see Fig. 2C). When the ribbon is fully occupied with vesicles and there is no evoked release of vesicles (i.e., holding the bipolar cell at -65 mV), there will be one vesicle per release site that is "docked" at the presynaptic membrane. We adopt the terminology for the sum of the docked vesicles at a ribbon synapse as the ultrafast pool (UFP, Fig. 2C) (Heidelberger, 2001; Mennerick and Matthews, 1996; von Gersdorff et al., 1996). For example, for the tiger salamander bipolar terminal schematized in Fig. 1C, there are five rows of vesicles yielding an RVP of 5 and 5 release sites on each side of the ribbon, resulting in a UFP of 10 vesicles. So, when the ribbon is fully populated with vesicles, the RVP will include one vesicle that is also considered a member of the UFP. The total tethered vesicles on a ribbon is RVP $\times$ UFP.

We have chosen to model the ribbon synapse with the assumption that the locations of the docked vesicles represent sites for vesicle fusion. We favor this approach for its heuristic appeal and because using multiple release sites is consistent with ultrastructural freeze fracture data (Roberts, 1994; Roberts et al., 1990). While we assume that each release site is independent of release at other sites at the ribbon, the model can be easily modified to test hypotheses such as correlated simultaneous vesicular release (Singer et al., 2004)

or the possibility of different pools of vesicles having calcium sensors that differ in their sensitivity to calcium as described next.

The program can specify a different rate of release for different pools of vesicles as suggested by physiological studies (Gomis et al., 1999; Mennerick and Matthews, 1996; Neves and Lagnado, 1999; von Gersdorff et al., 1996). It has been proposed that docked vesicles (UFP) are exposed to a higher level of calcium than the other tethered vesicles as they are located closer to the presynaptic calcium channels and therefore have a higher rate of exocytosis. To achieve this behavior, at each time step of a simulation, the program calculates the calcium concentration at two distances from the membrane (d_1 and d_2); one is applied to the UFP and the other for the remainder of the RVP (see Eqs. (4) and (5)). The program can also allow for different calcium buffering at these two distances by setting the time constants of removal (τ_{d_1} and τ_{d_2}).

Consistent with concept of vesicular release being driven by calcium sensors at different distances or having different calcium affinities, exocytosis measured via capacitance in the goldfish giant bipolar terminal evoked by depolarizing steps of different durations has been described by dual-exponential functions (Burrone and Lagnado, 2000; Mennerick and Matthews, 1996). This finding can be expressed as

$$\Delta C_m(t) = C_{1max}(1 - e^{-RC_1 t}) + C_{2max}(1 - e^{-RC_2 t}) \qquad (2)$$

where C_{1max} is the capacitance of the docked vesicles at time t and C_{2max} the capacitance of the tethered, non-docked vesicles remaining in the terminal. Making the simplifying assumption that all ribbons have the same size, Eq. (2) can be applied to a single ribbon or even a single release site by scaling the size of the asymptotic capacitance to the smaller structures. In our model since capacitance changes are discrete, based on the assumption of a fixed size of each vesicle, we make calculations based on the number of vesicles rather than capacitance.

Differentiating Eq. (2) provides the rate of release at any time, t, which depends on the rate constant derived from the Hill equation from Fig. 4 and the proportion of vesicles remaining in the two pools:

$$\text{Release rate (vesicles/s/terminal)} = \frac{dC_m}{dt}$$
$$= RC_1(t) \times \text{UFP}(t) + RC_2(t) \times \text{RVP}(t) \qquad (3)$$

To model this behavior, the program calculates the Rate for each release site in the simulation using the following conditional equations:

If $\text{RVP}(t) = \text{RVP}_{max}$ then Rate(vesicles/s/release site)
$$= RC_{d_1}(t) \times \text{UFP}(t) \qquad (4)$$

If $\text{RVP}(t) < \text{RVP}_{max}$ then Rate(vesicles/s/release site)
$$= RC_{d_2}(t) \times \text{RVP}(t) \qquad (5)$$

where $RC_{d_1}(t)$ and $RC_{d_2}(t)$ are the rate constants as determined by $[\text{Ca}^{2+}](t)$ at distances d_1 and d_2, respectively.

1.5. Exocytotic mechanism – stochastic determination of release events

The instantaneous release rate (Rate) from Eq. (4) or (5), expressed as the release in vesicles per second per release site, is applied independently and stochastically to each release site by using the conditional expression:

$$\text{Random}(0\text{–}1) \leq \text{Rate}/(1000/\,dT) \qquad (6)$$

At each time step, in Eq. (6) for dT in ms, the expression is evaluated and, if true, a vesicle is released and the size of either the UFP or RVP is decremented. Rate is normally controlled by the $[\text{Ca}^{2+}]$ to RC function as shown in Fig. 4, but it can also be set to a constant or other time-varying function for testing purposes. The model also includes a refractory period for the release sites. The current implementation lets the user set the duration of an absolute refractory period which is applied to all release sites. For simulations run in this study, this refractory period was set to zero.

1.6. Exocytotic mechanism – replenishment of tethered vesicles

Vesicles are added to the RVP for each release site using the following algorithm:

$$\text{rRate (vesicles/s)} = (\text{RVP}_{max} - \text{RVP}(t))$$
$$\times \text{ replenishment rate constant (rRC)}$$
$$(7)$$

The conditional expression of Eq. (6) is applied to make the replenishment of vesicles stochastic by substituting rRate for Rate. This function yields an exponential replenishment as a function of time (see Fig. 8C).

1.7. Exocytosis – diffusion of neurotransmitter

The concentration of neurotransmitter in and near the synaptic cleft resulting from a released vesicle was obtained by three-dimensional Monte Carlo diffusion modeling using MCell (Stiles and Bartol, 2001). We chose this approach because the ribbon synapse between salamander bipolar and ganglion cells occurs in what is termed a "dyad" arrangement in which one bipolar cell presynaptic ribbon is apposed to two postsynaptic dendritic processes. MCell tracks the diffusion of transmitter with a specification of the geometry of the dyad and the location of the release site along the ribbon (see Fig. 2B and C).

Many other parameters which will influence the neurotransmitter reaching the postsynaptic receptors are also variables in MCell including: quantal content, diffusion rate, the tortuosity and volume fraction of the tissue and the presence

and kinetics of pre- and postsynaptic receptors and transporters. Since the purpose of this paper is to describe the model, we report simulation behavior for a single set of MCell parameters. A more detailed description of the effects of parameter variation on the neurotransmitter spatiotemporal concentration profile is in preparation (Gottesman, personal communication).

The MCell parameters we used embedded a dyad ribbon synapse in a 18-μm^3 volume of schematized inner plexiform layer (IPL) composed of 125 separate "cellular processes". Two thousand molecules of glutamate (diffusion rate = $1.0 \times 10^{-6} \, cm^2/s$) were released from the presynaptic terminal into this IPL which had a synaptic cleft and extracellular space 20 nm wide, a tortuosity of 1.4 and a volume fraction of 0.13. Measurement of the glutamate concentration included the fact that surfaces in the IPL had ligand-gated channels and/or glutamate transporters that could bind the diffusing ligand. The data were generated with 1 μs time steps using MCell and Fig. 2B and C is images of the simulation geometry at the dyad (Gottesman and Miller, 2003a, 2004). To allow consideration of the spillover hypothesis of NMDA activation at the ribbon synapse (Matsui et al., 1998; Miller et al., 2001a,b), we measured the average glutamate concentration at the site of release and also at a distance of 250 nm from that site as shown by the solid gray lines in Fig. 5.

We have previously reported that if multiple release sites exist along the ribbon, a shift in the spatial location of exocytosis of 50 nm gives rise to differences of approximately
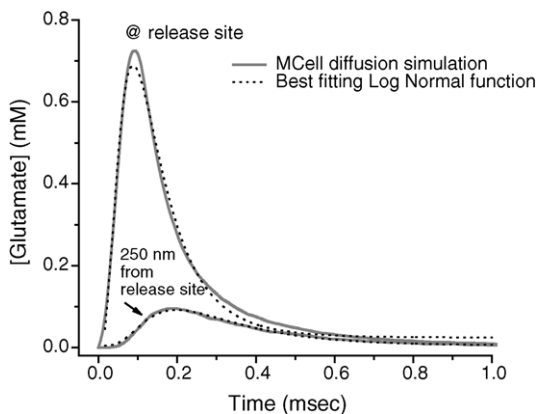

Fig. 5. Simultaneous glutamate profiles (solid gray lines) derived from MCell runs assuming receptors directly underneath the release site and displaced 250 nm from the release site. The data plotted are the mean concentration values averaged from 200 simulation runs. The diffusion rate was $1.0 \times 10^{-6} \, cm^2/s$. Quantal content was 2000 molecules released from a vesicle 25 nm in diameter (vesicular concentration = 405 mM). Release was through a fusion pore 10 nm long that opened at a rate of 25 nm/s (Stiles et al., 1996). These glutamate profiles as a function of time (t) were approximated by a log normal function for implementation in the model (dotted lines): Glu = $(A/\sqrt{2\pi}(wt)) \times e^{-[\ln(t/t_p)]^2/2w^2}$. The proximal (AMPA) site was characterized as a log normal function with an amplitude $A = 0.124$, time to peak (t_p) = 0.135 ms and width $w = 0.672$ ms. The distal (NMDA) site was characterized as a log normal function with $A = 0.035$, $t_p = 0.297$ ms and $w = 0.634$ ms.

14% in the peak neurotransmitter stimulus seen by a spatially fixed population of postsynaptic receptors (Miller et al., 2001a,b). These transmitter concentration differences will give rise to simulated quantal excitatory postsynaptic conductance (EPSC) variations that depend upon the kinetic model of postsynaptic receptors as well as their number and density on the postsynaptic membrane. With our use of 128 receptors using the 6-state AMPA receptor model (see below), the differences, as a function of release site, in simulated EPSC amplitude are less than 1 pA for the most extreme case. Because of these small differences, we chose to simplify the model by presenting a single transmitter stimulus for all release sites. Modeling other ribbon synapses that require different assumptions about the release site geometry or postsynaptic receptor numbers and kinetics may require specification of the transmitter stimulus arising from each location. Our model can easily be extended to incorporate these differences in transmitter concentration that depend on where, along the ribbon, a vesicle is released.

In order to have multiple ribbon synapses onto a single ganglion cell, NEURON requires the glutamate concentration changes following a release event (simulated quantal release) be expressed as an analytic function. We do this by approximating the diffusion data with a log normal function that was used solely for computational convenience. The dotted lines in Fig. 5 display the glutamate time course for vesicular release in our ribbon synapse model, implemented as the best fitting log normal functions matched to the diffusion modeling results. Each release event at a ribbon gives rise to these glutamate transients and the glutamate is summed across time for events at each ribbon.

A second reason for using the log normal function is so that the user can alter the characteristics of the neurotransmitter stimulus without having to run MCell simulations. For example, to simulate a faster diffusion rate, the log normal function amplitude and width would be reduced and the time to peak shortened. While this function provided excellent approximation to the MCell data ($r^2 \geq 0.99$ for 24 different parameter conditions, Gottesman, personal communication), it should be noted that the user can replace the log normal function with any relationship deemed appropriate to characterize the spatiotemporal concentration of transmitter for their synapse.

1.8. Postsynaptic response – ligand-gated receptors

The glutamate stimuli in Fig. 5 drive the behavior of kinetic models of AMPA (glutamate at the release site) and/or NMDA receptors (glutamate at 250 nm from the release site). The choice of the number of model states, transition rates and maximum conductance is under the experimenter's control.

AMPA receptor kinetics were modeled using the 6-state scheme of Partin et al. (1996). To estimate the AMPA maximum conductance (AMPA$_{gmax}$) at each active zone we assumed a channel density of 5000 channels per square micron.

EM analysis of serial sections of the salamander postsynaptic density yielded a surface area of approximately $0.0256 \, \mu m^2$, which would yield 128 AMPA channels. This would result in an $AMPA_{gmax}$ of 1.28 or 2.56 nS, assuming a single-channel conductance of either 10 or 20 pS, respectively.

The 5-state NMDA kinetic scheme of Hessler et al. (1993) was utilized and presumed the presence of 0.5 mM Mg^{2+} and a tonic level of $1 \, \mu M$ glutamate in the extracellular space. NMDA maximum conductance ($NMDA_{gmax}$) ranged from 55 to 170 pS, depending on the number of synapses present in the simulation. $NMDA_{gmax}$ was set 10 pS below the density that, when NMDA was the only receptor present, just gave a spiking response to the bipolar stimulus. We modeled the glycine-binding site of the NMDA receptor as being saturated, but see Stevens et al. (2003) for consideration of this assumption.

1.9. Postsynaptic response – ganglion cell anatomy, passive and active membrane properties

The conductance changes resulting from activation of these glutamate channels will depolarize an experimenter-defined computational model of a postsynaptic cell which can be as simple as a single electrotonic compartment, an equivalent cylinder or a computational structure derived from traced cell morphology. For our simulations, the anatomy of a sustained ON ganglion cell stained by intracellular dye injection was measured and reconstructed using the Eutectic tracing system. The Eutectic data were converted to an electrotonic model via the Asc2nrn program (http://www.cns.unibe.ch/asc2nrn/). This structure was imported into NEURON and stimulated at multiple locations on the dendritic tree (Fig. 6). An axon was included in the geometry with parameters identical to those published by Fohlmeister and Miller (1997). Compartment size was $10 \, \mu m$ throughout. Passive properties were defined for all simulations using a reversal potential of $-65 \, mV$, a membrane conductance of $1/70,000 \, S/cm^2$ and an axial resistance of $110 \, \Omega \, cm$. Active channel densities followed those of Fohlmeister and Miller (1997) for their 'EC2.5 REAL' model. The postsynaptic cell resting potential at the soma was $-65.8 \, mV$ with all channels present and $-66.6 \, mV$ with the Na^+ channel removed (for simulation of experiments in tetrodotoxin, TTX).

2. Results

2.1. Modeling flash photolysis of caged calcium

We ran simulations of flash photolysis experiments in which ATP is omitted from the intracellular solution thus preventing any replenishment of vesicles to the ribbon (Heidelberger et al., 1994, 2002; Thoreson et al., 2004). Under these conditions, the model bipolar cell compartment can be stimulated with an instantaneous step of calcium, mimick-
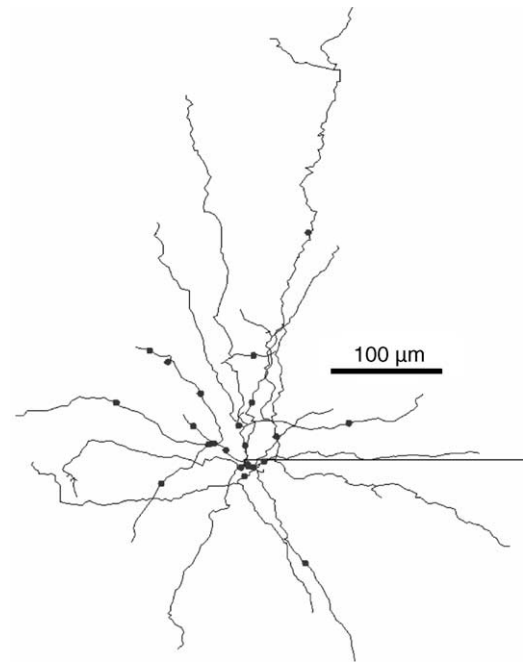

Fig. 6. The Eutectic traced reconstruction of the HRP-stained sustained ON ganglion cell used in the simulations. The 23 dots show the placement of ribbon synapses. From 2 to 6 ribbons were placed in the compartment shown by each location (see Fig. 10).

ing the release of caged calcium. Fig. 7 shows the results of four such simulation runs at four different levels of calcium. The bipolar terminal was modeled as a goldfish giant bipolar terminal in which there were 50 ribbons, each ribbon had 20 release sites and each release site had an RVP_{max} of five vesicles. The simulation data (open circles) are fit with a single exponential function ($r^2 > 0.999$ for all panels) and the rate constants obtained from these fits are in excellent agreement with the data of Heidelberger et al. (1994). The values of RC for these four simulations are also plotted as filled circles in Fig. 4. The correspondence between model and the data of Fig. 4 is not surprising since the algorithm that underlies the simulation release process is derived from the Hill function fit to the original raw data of Heidelberger et al. (1994).

2.2. Modeling release as a function of pulse duration

Several investigators have reported on the exocytosis at the goldfish giant bipolar terminal using voltage clamp steps of different duration to depolarize the membrane, activating calcium channels (Burrone and Lagnado, 2000; Gomis et al., 1999; Mennerick and Matthews, 1996; Neves and Lagnado, 1999; von Gersdorff and Matthews, 1994). Fig. 8A shows the results of simulations using the identical parameters as for the flash photolysis modeling. In this case, exocytosis is measured in response to calcium changes evoked by stepping the membrane potential from -65 to $0 \, mV$. Pulse duration was varied from 0.5 to 500 ms and the mean number of release events for 10 simulation runs are plotted as the open squares
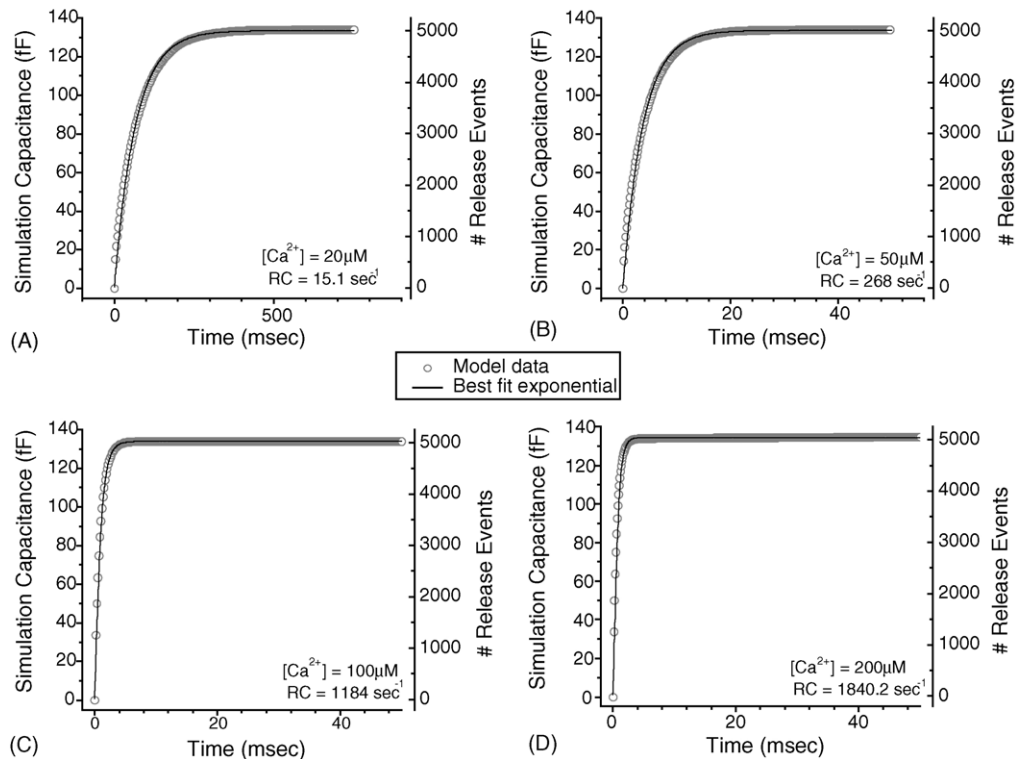
Fig. 7. Simulation of experiments with flash photolysis of caged calcium to instantly and uniformly fill the presynaptic terminal with different Ca^{2+} concentrations. At time zero, the calcium concentration is stepped to one of four values (20, 50, 100 and 200 μM) in a single compartment containing 50 ribbons each having 20 release sites and an RVP of 5. This yields 5000 tethered vesicles and a UFP for the terminal of 1000 vesicles. The replenishment rate of vesicles onto the ribbon (rRC) was set to zero to mimic the absence of ATP in the intracellular electrode solution. The open circles plot the mean number of release events (right ordinate) for 10 model runs. For all panels in this and subsequent figures, the standard deviations of the means are smaller than the symbol size used. For comparison with the results of Heidelberger et al. (1994), we scaled these release events assuming a single vesicle capacitance of 26.8 aF and those values are plotted on the left ordinate. The solid line in each graph is a single exponential function which best fits the simulation data. The values of the calcium concentration and corresponding rate constants are shown for each graph. Model parameters were: L channel conductance density = 0.0012 S/cm^2; the depth of the calcium shell is not relevant as flash photolysis generates uniform calcium throughout the cell. Calcium removal was set to zero since calcium levels resulting from photolysis do not fall for 2 s post flash (Heidelberger et al., 1994).

in Fig. 8A. The solid line is the best-fit ($r^2 = 0.994$) dual-exponential function to these data.

The fast component at short durations is fit by an exponential with a time constant of 1.54 ms and an asymptotic capacitance of 1024 vesicles. This is consistent with release from the UFP, which has a size of 1000 in these simulations and whose release rates were driven by the calcium concentration 25 nm from the membrane. This value agrees well with experimental capacitance measurements reporting a fast time constant in the range 1.3–2.6 ms (Burrone and Lagnado, 2000; Gomis et al., 1999; Mennerick and Matthews, 1996; Neves and Lagnado, 1999).

The slower second phase of release is fit by an exponential function with a time constant of 376 ms and a maximal release of 4538 vesicles. This corresponds approximately to the remaining tethered vesicles on the ribbon ($n = 4000$, without consideration of replenishment) whose release rates were driven by the calcium concentration 50 nm from the membrane. The time constant of release agrees well with the data of Mennerick and Matthews (1996, $\tau = 349$ ms). It is faster than the values reported by Lagnado and colleagues (Burrone

and Lagnado, 2000; Neves and Lagnado, 1999) of from 500 to 970 ms and we did not attempt to modify the model parameters to obtain behavior in that range.

The maximal rates of release evoked by voltage steps observed experimentally are limited by the activation kinetics of the calcium channels (Mennerick and Matthews, 1996). This can be demonstrated by using a voltage protocol that steps to a voltage that activates the calcium channels without any calcium influx and then subsequently stepping to a new voltage that is accompanied by influx. We modeled this by a voltage protocol that stepped to +120 mV (the reversal potential for calcium in the model) for 500 ms and then stepped to 0 mV for durations ranging from 0.1 to 2.5 ms and then finally stepping to −65 mV closing the channels. As a control we verified that stepping from +120 to −65 mV did not evoke any vesicle release from the model.

Fig. 8B plots the mean number of release events as a function of the time spent at 0 mV (open squares). The data are well fit ($r^2 = 0.97$) by a single exponential function with a time constant of 0.6 ms. This increase in the rate of release, compared to the value of 1.54 ms obtained without using the

prepulse to open the L-type channels, is in excellent agreement with the experimental data, which showed a $\tau = 0.5$ ms (Mennerick and Matthews, 1996).

2.3. Modeling paired pulse depression in bipolar terminals

Numerous laboratories have observed paired pulse depression in capacitance measurements of exocytosis at ribbon synapses (Burrone and Lagnado, 2000; Eisen et al., 2004;

(A)

(B)

(C)

Gomis et al., 1999; Mennerick and Matthews, 1996; Moser and Beutner, 2000; von Gersdorff and Matthews, 1997). Simulations were run using the protocols of Mennerick and Matthews (1996) and von Gersdorff and Matthews (1997) in which two depolarizing steps from −65 to 0 mV were separated by a varying interstimulus interval. Fig. 8C shows that the model replicates the single exponential time course of recovery of the capacitance responses in these different paired pulse experiments by changing the time course of the replenishment of vesicles on the ribbon as set by the value of rRC.

2.4. Modeling bipolar cell excitatory inputs to ganglion cells

We examined the effect of variations in the strength of synaptic inputs to the salamander ganglion cell and an example of the process is shown in Fig. 9 for conditions in which there were five ribbon synapses located at each site indicated in Fig. 6. Each synapse had 10 release sites and the postsynaptic $AMPA_{gmax}$ was 2.56 nS. Panel A shows a typical light-evoked response elicited by a small, centered white light stimulus on a dim background obtained via whole-cell recording in an intact eyecup from the soma of a depolarizing (Bd) bipolar cell. This record was used as the dynamic command voltage for a voltage-clamp in a compartment, representing the Bd terminal, containing the L-type voltage-gated calcium channel of Fig. 3. Panel B shows the calcium concentration at 25 nm (black line) and 50 nm (gray line) from the 'membrane'. The 25-nm calcium 'microdomain' response evoked by the Bd voltage reaches a peak of 13.2 μM. Resting $[Ca^{2+}]$
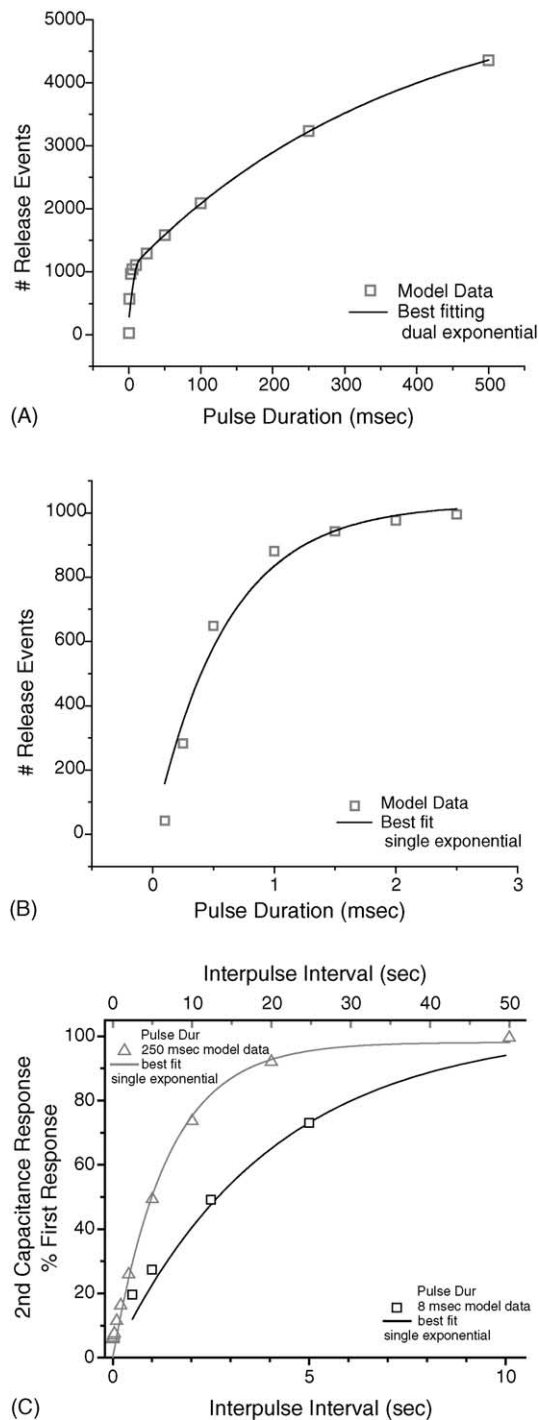

Fig. 8. (A) Simulation of exocytosis evoked by voltage steps in the presynaptic compartment from −65 to 0 mV for durations ranging from 0.5 to 500 ms. The open squares are the mean of 10 model runs. These data were well fit ($r^2 = 0.994$) by the sum of two exponential functions plotted by the solid line. The fast time constant was 1.54 ms and the slower time constant was 376 ms. The model parameters were: L channel conductance density = 0.0012 S/cm²; $d_1 = 25$ nm; $\tau_{d_1} = 0.8$ s; $d_2 = 50$ nm; $\tau_{d_2} = 0.3$ s and replenishment rate (rRC) was set to 0.125 s⁻¹. (B) Simulation demonstrating that the kinetics of the L-type calcium channel limit the release of vesicles replicating the experiment of Mennerick and Matthews (1996, Fig. 4). In voltage clamp, the membrane potential is stepped to the reversal potential for Ca^{2+} (+120 mV) for 500 ms. Then the membrane is stepped to 0 mV for varying durations (0.1–2.5 ms) before the voltage is stepped to −65 mV. Release events are evoked during the pulse at 0 mV as the driving force for calcium influx is restored. The open squares show the mean number of release events ($n = 10$) at each pulse duration at 0 mV and these data were well fit ($r^2 = 0.97$) by a single exponential with a time constant of 0.6 ms. Model parameters identical to those in panel (A). (C) Simulations demonstrating the replenishment of vesicles onto the ribbon via a paired pulse protocol. Two 8 ms (squares and lower abscissa) or 250 ms (triangles and upper abscissa) voltage steps from −65 to 0 mV are applied to the model separated by a variable interpulse interval. The symbols plot the mean ($n = 10$) relative size of the second pulse when compared to the first pulse as a function of the time between the steps. The solid black curve is the best-fit single exponential for the 8-ms pulses which has a time constant of 3.1 s ($r^2 = 0.987$). Model parameters identical to panel (A). The solid gray line is the single exponential fit to the data for 250-ms pulses which has a time constant of 6.86 s ($r^2 = 0.986$): Model parameters identical to those in panel (A) except rRC = 0.25 s⁻¹.
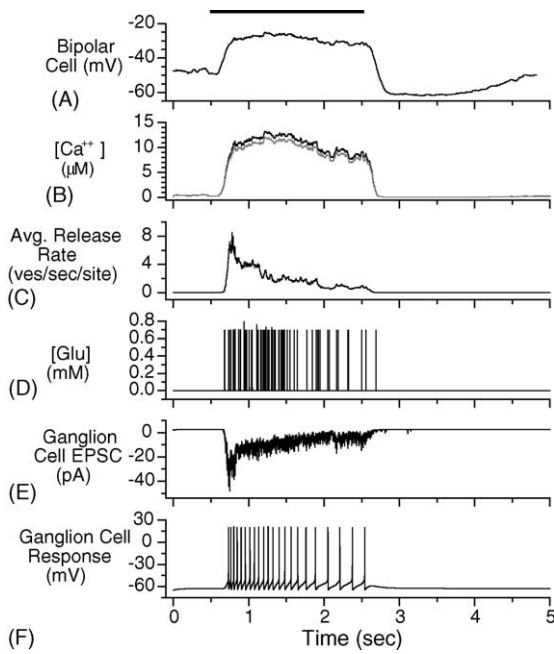
Fig. 9. (A) A whole-cell voltage recording from the soma of a salamander ON bipolar cell stimulated with a centered spot +1 log unit above a 20 cd/m^2 background. The stimulus timing is indicated by the dark bar above the figure. Model parameters for the bipolar terminal were: L channel conductance density = 0.0012 S/cm^2; d_1 = 25 nm; τ_{d_1} = 0.8 s; d_2 = 50 nm; τ_{d_2} = 0.3 s; rRC = 0.25 s^{-1}. (B) The resultant calcium concentration sensed at 25 (black) and 50 (gray) nM from the 'membrane' of the presynaptic cell. [Ca^{2+}] at 25 nm peaks at 13.2 μM and rests prior to stimulus at about 0.43 μM. (C) The average rate of exocytosis at a release site. The response peaks at a rate of 8.5 and rests at 0.0006 vesicles/s/release site. The release rate of a ribbon is the summed release from the number of sites defined for the ribbon. (D) Glutamate release for an entire ribbon synapse. Shown are only the AMPA profiles (see Fig. 5). Due to the stochastic nature of release in the model, this is only an example from a 10-release-site synapse driven by the rate function in panel (C). (E) The EPSC when the soma is voltage-clamped at −65 mV (Na$^+$ channels turned off to simulate the presence of TTX) resulting from the stimulation of AMPA and NMDA channels. (F) The light-evoked spiking in the soma of the postsynaptic ganglion cell.

on the dim background is 0.43 μM. The calcium concentration at each time step is converted to a rate of vesicle fusion at each release site using Eq. (4) or (5) and the result for this simulation is illustrated in panel C. The glutamate concentration resulting from stochastic release from the presynaptic terminal is shown in panel D. The glutamate from individual exocytotic events rises and falls in less than a millisecond resulting in the 'spike' appearance at the time scale used for the figure. Panel E shows the EPSC at the soma (voltage-clamped at −65 mV) resulting from the release events of panel D and somatic current clamp spiking is shown in panel F. The model produces sustained spiking during Bd cell depolarization.

The model displays a transient rate of release (Fig. 9, panel C) of vesicles even in the presence of a maintained membrane depolarization and maintained elevation in calcium concentration (Fig. 9, panels A and B). This reduction in release rate is solely the result of the depletion in the size of both the UFP and RVP and not any change in calcium channel

behavior as the model does not contain any mechanisms to alter the non-inactivating character of the L-type channels.

Simulation runs were carried out with for two values of AMPA$_{gmax}$ (1.28 or 2.56 nS), the presence or absence of NMDA receptors and a variable number of ribbons contacting the ganglion cell (46–138). The voltage stimulus was kept constant, resulting in the same calcium influx and release rate for the synapses (i.e. traces A–C in Fig. 9 are constant for all simulations). All things being equal, an increase in any one of the varied parameters was expected to increase the firing rate of the ganglion cell.

When only AMPA receptors are present there is no spiking or weak spiking evoked by stimulation from 46 to 138 synapses (Fig. 10, panels a–j). When only NMDA receptors are present there is no evoked spiking regardless of the number of synapses in the simulation (data not shown). However, the presence of NMDA receptors does facilitate the modeled light-evoked response as shown in the right column of Fig. 10. When AMPA receptors were combined with NMDA receptors an increase in firing compared to AMPA alone was seen under all conditions.

2.5. Desensitization of AMPA receptors reduces model ganglion cell responses

We ran simulations to explore the effect of reducing desensitization of AMPA receptors. We modified the kinetic model of the AMPA receptor to include 12 states having transition rates that depended on the concentration of cyclothiazide (Partin et al., 1996). We show one example of the effect of reducing AMPA desensitization in Fig. 11. The black trace is the simulated excitatory post synaptic potential (sEPSP) evoked by 115 ribbon synapses placed on the ganglion cell and these synapses were driven by the ON bipolar light-evoked voltage shown in Fig. 9A. The gray trace is the sEPSP to the same stimulus, but in the presence of 30 μM cyclothiazide. The reduction of the desensitization results in a response that is more than double the size of the "control" response suggesting there is substantial AMPA desensitization produced by the ribbon synapse input from the sustained ON bipolar cell.

The inset in Fig. 11 shows the simulated miniature EPSP (smEPSP) evoked by quantal release. The normal response shown by the black trace is smaller and faster than that obtained in the presence of 30 μM cyclothiazide similar to the result in salamander ganglion cells using 2 mM aniracetam (Taylor et al., 1995).

3. Discussion

The ribbon synapse model presented in this paper is designed to be used in simulating the synaptic input to cells postsynaptic to neurons possessing these specialized structures. Using a single set of parameter values, the presynaptic portion of the model succeeds in replicating experimental findings in
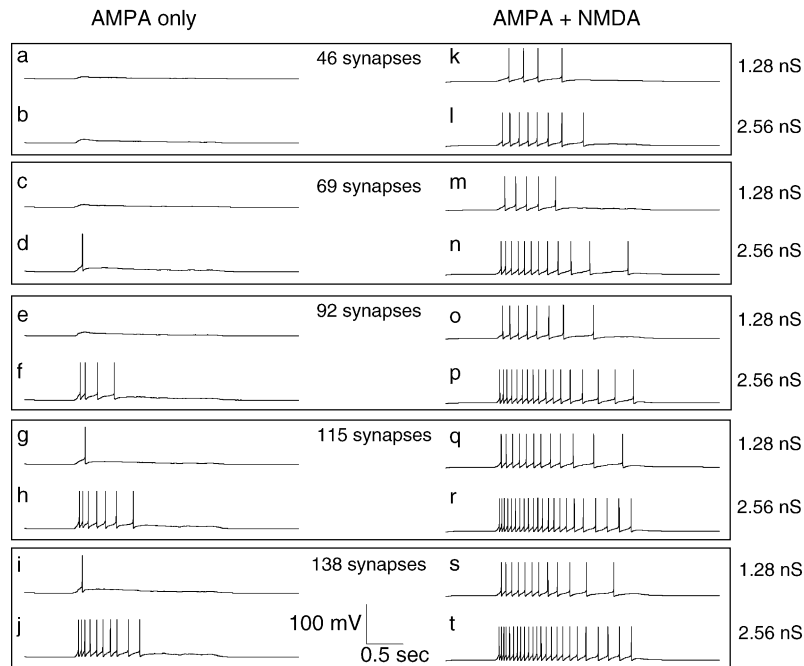
Fig. 10. Spike trains in the soma of the model ganglion cell varying two parameters. (1) The maximum conductance of the AMPA receptors (1.28 or 2.56 nS); (2) the total number of ribbon synapses placed on the model ganglion cell dendritic tree (46–138). The left column shows spiking responses for excitation from AMPA alone and the right column excitation from AMPA plus NMDA receptors. The NMDA$_{gmax}$ was decreased as the total number of synapses increased so no spiking was evoked if NMDA receptors were stimulated alone. For 46 synapses, gmax = 170 pS; for 69, gmax = 110 pS; for 92, gmax = 85 pS; for 115, gmax = 75 pS and for 138, gmax = 55 pS.

the goldfish giant bipolar terminal for exocytosis produced by either release of caged calcium (Heidelberger et al., 1994) or depolarization (Burrone and Lagnado, 2000; Mennerick and Matthews, 1996; von Gersdorff and Matthews, 1997) via the implementation of two pools of vesicles. This is consis-
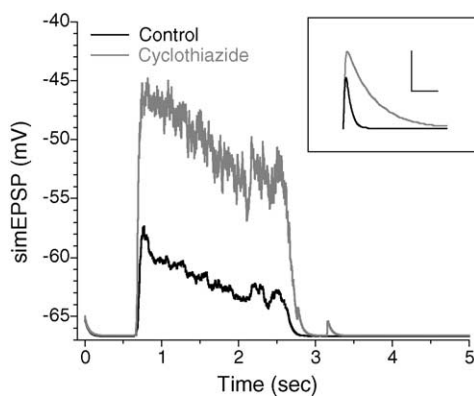

Fig. 11. Simulated EPSPs elicited by 115 ribbon synapses having 10 release sites as in Fig. 9E. Na$_{gmax}^{+}$ was set to 0. AMPA$_{gmax}$ = 1.28 nS and NMDA$_{gmax}$ = 170 pS. The black trace is the control simulated EPSP driven by the light-evoked ON bipolar voltage response shown in Fig. 9A activating AMPA + NMDA receptors. The gray trace uses the identical stimulus but the kinetic model of AMPA receptors was modified by the presence of 30 μM cyclothiazide using the scheme of Partin et al. (1996). Inset: simulated mEPSPs. The black trace is the control mEPSP and the gray trace is the mEPSP in the presence of cyclothiazide. Scale bars are 5 ms and 0.009 mV.

tent with the idea that these pools would correspond to those vesicles docked at the presynaptic membrane (UFP) and the remaining vesicles tethered to the ribbon (the release ready pool, Heidelberger, 2001).

We applied the same model parameters used to replicate the goldfish bipolar terminal data to our model of the tiger salamander bipolar cell. The only change required was to reduce the number of release sites at each ribbon to a value of 10 versus 20 used for the goldfish. Using realistic profiles for glutamate diffusion from three-dimensional Monte Carlo modeling, we simulated the postsynaptic response of ganglion cells by placing a relatively small number of ribbon synapses on the dendritic tree of a morphologically realistic salamander ganglion cell possessing a five voltage-gated channel active membrane. The glutamate released by the presynaptic mechanism drove the conductance of kinetic models of AMPA and NMDA receptors on the ganglion cell.

The example presented here of the depolarizing bipolar cell to sustained ON ganglion cell synapse in the salamander retina successfully shows firing of action potentials in response to light-evoked depolarization of the bipolar cell. The model parameters producing this response were constrained by anatomical measurements of the dimensions of the ribbon and vesicles found in the bipolar terminal, reported *I–V* characteristics of L-type calcium channels associated with vesicular release and the size of the postsynaptic density found at the dyad synapse.

3.1. Ribbon release sites do not have especially high rates of release

While ribbon synapses have been touted for their high rates of release (Heidelberger et al., 1994; Matthews, 1999; von Gersdorff and Matthews, 1994, 1997), these simulations make clear that the power of the bipolar cell to ganglion cell synapse derives mostly from the number of release sites contained in the bipolar cell axon terminal. For the goldfish giant bipolar terminal, the ability to release thousands of vesicles per second is a consequence of having up to 100 ribbons per terminal and the presence of 12–24 release sites per ribbon. In the salamander bipolar cell, the terminal size is much smaller and inputs to the ganglion cell from multiple bipolar cells would be needed to achieve the number of synapses modeled in Fig. 10.

The issue is embodied in the model's calcium concentration to release rate function expressed by Eqs. (4) and (5). When one scales the release rate for an entire terminal to the number of release sites in the terminal, the instantaneous maximum release rate at any single release site in response to a step depolarization to the maximum L channel activation voltage is approximately 60 Hz. This reflects the fastest release rates when the UFP is full. However, release rates in the presence of maintained depolarization are substantially slower as this pool is depleted. Fig. 9C provides an example of this: the relatively maintained light-evoked depolarization of the ON bipolar cell evokes a transient rate of release from the presynaptic terminal.

The model's maximum rate at individual ribbon release sites is similar to the maximal release rate of 50 Hz observed at non-ribbon CNS synapses (Stevens and Wang, 1995). This suggests that the high rate of release exhibited by the giant bipolar terminal is not based on specialized exocytotic machinery for the ribbon synapse. Instead, it is likely to be the result of having multiple release sites per active zone and larger pools of readily releasable and available vesicles.

3.2. Ribbon synapse vesicular release has transient and sustained components

The data shown in Fig. 9 (panels C–F) demonstrate that the release of vesicles at the ribbon synapse as modeled in this paper displays an initial transient high rate of release followed by a slower, more sustained rate of exocytosis. This behavior occurs while the membrane depolarization (Fig. 9, panel A) and calcium influx (Fig. 9, panel B) are fundamentally sustained. The reason for the transient nature of release is the depletion of the vesicle pools and subsequent reduction in release rate as expressed in Eqs. (4) and (5). The maintained slower rates of release in this model represent the equilibrium established between exocytosis and replenishment of vesicles back onto the ribbon.

Our demonstration of transient and sustained elements in ganglion cell responses to bipolar cell input at the ribbon synapse are qualitatively similar to numerous reports in the literature (Higgs and Lukasiewicz, 1999; Lukasiewicz et al., 1995; Matsui et al., 1998; Singer and Diamond, 2003). Our model possesses two mechanisms for producing the transient nature of ganglion cell responses to sustained bipolar cell depolarization: the reduction in presynaptic release described above and the postsynaptic desensitization of AMPA receptors as shown in Fig. 11. There are several other mechanisms that can contribute to the production of transient responses in ganglion cells which are not yet part of our model. These include a depolarizing shift in the activation voltage of calcium channels induced by GABAergic inputs (Heidelberger and Matthews, 1991), inhibition of bipolar cell release via hyperpolarization evoked by opening of chloride channels gated by GABA (Hartveit, 1999; Lukasiewicz and Werblin, 1994; Matsui et al., 2001), inhibition of calcium channels by acidification of the synaptic cleft resulting from exocytosis (Palmer et al., 2003) and inhibition of release resulting from activation of presynaptic metabotropic receptors (Higgs et al., 2002).

3.3. Ganglion cell excitation does not require many ribbon synapses

The spatial extent of the excitatory receptive field in the salamander ganglion cell has been estimated to be approximately 100 μm in diameter (Lukasiewicz and Werblin, 1990), but there are no definitive quantitative studies of the retinal anatomy of the salamander that address the number of excitatory bipolar to ganglion cell synapses. In the cat retina the number of excitatory synapses can range from 150 to 2000 depending on the ganglion cell type and the amount of dendritic area (Freed, 2000). Miller et al. (2001), using activity-dependent dyes, reported a range of 18–76 contacts per 1000 μm^2 onto salamander ganglion cells. The sustained ON ganglion cell modeled (Fig. 6) had a dendritic surface area of 5622 μm^2 which would lead to an estimate of 101–427 synapses. What proportion of these is excitatory is unknown. Also, if the excitatory inputs are not found over the entire dendritic tree, this would further reduce the number of inputs. We used a range of 46–138 excitatory synapses, the majority of which are within 100 μm from the soma, in an attempt to bracket excitatory synaptic density in the salamander. When excitation of both AMPA and NMDA receptors are included in the model, sustained firing of action potentials is evoked by as few as 46 ribbon inputs to the ganglion cell.

The importance of NMDA input in producing robust spiking in the ganglion cell results from two NMDA-dependent components. First, there is a tonic depolarization (approximately 2.7 mV) resulting from the presence of tonic glutamate (1 μM) in the extracellular space. The presence of tonic glutamate is consistent with the observation that NMDA channel noise is present in salamander ganglion cells in the presence of physiological levels of magnesium (Gottesman and Miller, 2003b). Second, even though the light-evoked glutamate-stimulating NMDA receptors is at a much lower level than that stimulating the AMPA receptors (see Fig. 5),

the higher affinity for glutamate and the large single-channel conductance of NMDA receptors both result in a light-evoked NMDA depolarization that combines with the AMPA response to result in a larger EPSP and concomitant greater excitation than when AMPA receptors alone are in the model.

3.4. AMPA desensitization is evoked by exocytosis from ribbons

It was unclear a priori if having multiple ribbons providing excitatory input to the ganglion cell would mean that no single active zone would show strong overlap of release events in time. If this were true it might be that the concentration and duration of glutamate at any single ribbon synapse resulting from the light-evoked depolarization of the ON bipolar might produce only modest desensitization of the AMPA receptors on the ganglion cells. However, substantial desensitization has been shown in voltage-clamp data for tiger salamander ganglion cell AMPA receptors (Lukasiewicz et al., 1995). Consistent with that finding, the model also displays strong AMPA desensitization as shown by the 120% increase in simulated mEPSP amplitude under conditions that strongly reduced desensitization (Fig. 11).

The present study has generated a model of the ribbon synapse of bipolar cells based on physiological data that has accumulated for the past 10 years. The model has been structured with variables for each step and function, so that it can be adapted to ribbon synapses, in rods and cones as well as ribbon synapses in hair cells. We developed this model and applied it to the anatomical features of bipolar cell synapses in the salamander retina and determined that this model could account for the glutamatergic activation of retinal ganglion cells whose realistic, multicompartmental morphology was derived from single cell staining experiments. The ribbon synapse included the participation of AMPA and NMDA receptors arranged so that the NMDA receptor contributions are perisynaptic, consistent with physiological studies. Our first-generation model has successfully replicated many of the experimental observations whose target has been the large multiribbon terminals of goldfish bipolar cells. Like any first-generation model, we believe that further enhancements and improvements in its fidelity can be achieved as we learn more about this fascinating synaptic structure from additional experimental work and input from our colleagues.

Acknowledgments

References

Burrone J, Lagnado L. Synaptic depression and the kinetics of exocytosis in retinal bipolar cells. J Neurosci 2000;20:568–78.

Burrone J, Neves G, Gomis A, Cooke A, Lagnado L. Endogenous calcium buffers regulate fast exocytosis in the synaptic terminal of retinal bipolar cells. Neuron 2002;33:101–12.

Dowling JE, Boycott BB. Organization of the primate retina: electron microscopy. Proc R Soc London B: Biol Sci 1966;166:80–111.

Eisen MD, Spassova M, Parsons TD. Large releasable pool of synaptic vesicles in chick cochlear hair cells. J Neurophysiol 2004;91:2422–8.

Fohlmeister JF, Miller RF. Mechanisms by which cell geometry controls repetitive impulse firing in retinal ganglion cells. J Neurophysiol 1997;78:1948–64.

Freed MA. Parallel cone bipolar pathways to a ganglion cell use different rates and amplitudes of quantal excitation. J Neurosci 2000;20:3956–63.

Gomis A, Burrone J, Lagnado L. Two actions of calcium regulate the supply of releasable vesicles at the ribbon synapse of retinal bipolar cells. J Neurosci 1999;19:6309–17.

Gottesman J, Miller RF. Modeling the localization of NMDA receptors on salamander ganglion cells. Abstract viewer, online. Program number 5138, ARVO, 2003a.

Gottesman J, Miller RF. *N*-methyl-D-aspartate receptors contribute to the baseline noise of retinal ganglion cells. Vis Neurosci 2003b;20:329–33.

Gottesman J, Miller RF. Modeling bipolar cell quantal release onto ganglion cells in a schematized IPL. Abstract viewer, online. Program number 1330, ARVO, 2003b.

Hama K. Some observations on the fine structure of the lateral line organ of the Japanese sea eel *Lyncozymba nystromi*. J Cell Biol 1965;24:193–210.

Hartveit E. Reciprocal synaptic interactions between rod bipolar cells and amacrine cells in the rat retina. J Neurophysiology 1999;81:2923–36.

Heidelberger R. Electrophysiological approaches to the study of neuronal exocytosis and synaptic vesicle dynamics. Rev Physiol Biochem Pharmacol 2001;143:1–80.

Heidelberger R, Heinemann C, Neher E, Matthews G. Calcium dependence of the rate of exocytosis in a synaptic terminal. Nature 1994;371:513–5.

Heidelberger R, Matthews G. Inhibition of calcium influx and calcium current by gamma-aminobutyric acid in single synaptic terminals. Proc Natl Acad Sci USA 1991;88:7135–9.

Heidelberger R, Matthews G. Calcium influx and calcium current in single synaptic terminals of goldfish retinal bipolar neurons. J Physiol 1992;447:235–56.

Heidelberger R, Sterling P, Matthews G. Roles of ATP in depletion and replenishment of the releasable pool of synaptic vesicles. J Neurophysiol 2002;88:98–106.

Hessler NA, Shirke AM, Malinow R. The probability of transmitter release at a mammalian central synapse. Nature 1993;366:569–72.

Higgs MH, Lukasiewicz PD. Glutamate uptake limits synaptic excitation of retinal ganglion cells. J Neurosci 1999;19:3691–700.

Higgs MH, Romano C, Lukasiewicz PD. Presynaptic effects of group III metabotropic glutamate receptors on excitatory synaptic transmission in the retina. Neuroscience 2002;115:163–72.

Hines ML, Carnevale NT. The NEURON simulation environment. Neural Comput 1997;9:1179–209.

Hines ML, Carnevale NT. NEURON: a tool for neuroscientists. Neuroscientist 2001;7:123–35.

Katz PS, Kirk MD, Govind CK. Facilitation and depression at different branches of the same motor axon: evidence for presynaptic differences in release. J Neurosci 1993;13:3075–89.

Kidd M. Electron microscopy of the inner plexiform layer of the retina in the cat and the pigeon. J Anat 1962;96:179–87.

Kosaka T, Ikeda K. Possible temperature-dependent blockage of synaptic vesicle recycling induced by a single gene mutation in *Drosophila*. J Neurobiol 1983;14:207–25.

Lenzi D, Crum J, Ellisman MH, Roberts WM. Depolarization redistributes synaptic membrane and creates a gradient of vesicles on the synaptic body at a ribbon synapse. Neuron 2002;36:649–59.

Lenzi D, Runyeon JW, Crum J, Ellisman MH, Roberts WM. Synaptic vesicle populations in saccular hair cells reconstructed by electron tomography. J Neurosci 1999;19:119–32.

Lenzi D, von Gersdorff H. Structure suggests function: the case for synaptic ribbons as exocytotic nanomachines. Bioessays 2001;23:831–40.

Lukasiewicz PD, Lawrence JE, Valentino TL. Desensitizing glutamate receptors shape excitatory synaptic inputs to tiger salamander retinal ganglion cells. J Neurosci 1995;15:6189–99.

Lukasiewicz PD, Werblin FS. The spatial distribution of excitatory and inhibitory inputs to ganglion cell dendrites in the tiger salamander retina. J Neurosci 1990;10:210–21.

Lukasiewicz PD, Werblin FS. A novel GABA receptor modulates synaptic transmission from bipolar to ganglion and amacrine cells in the tiger salamander retina. J Neurosci 1994;14:1213–23.

Maguire G, Maple B, Lukasiewicz P, Werblin F. Gamma-aminobutyrate type B receptor modulation of L-type calcium channel current at bipolar cell terminals in the retina of the tiger salamander. Proc Natl Acad Sci USA 1989;86:10144–7.

Matsui K, Hasegawa J, Tachibana M. Modulation of excitatory synaptic transmission by GABA(C) receptor-mediated feedback in the mouse inner retina. J Neurophysiol 2001;86:2285–98.

Matsui K, Hosoi N, Tachibana M. Excitatory synaptic transmission in the inner retina: paired recordings of bipolar cells and neurons of the ganglion cell layer. J Neurosci 1998;18:4500–10.

Matthews G. Synaptic mechanisms of bipolar cell terminals. Vision Res 1999;39:2469–76.

Mennerick S, Matthews G. Ultrafast exocytosis elicited by calcium current in synaptic terminals of retinal bipolar neurons. Neuron 1996;17:1241–9.

Miller RF, Fagerson MH, Staff NP, Wolfe R, Doerr T, Gottesman J, et al. Structure and functional connections of presynaptic terminals in the vertebrate retina revealed by activity-dependent dyes and confocal microscopy. J Comp Neurol 2001a;437:129–55.

Miller RF, Gottesman J, Henderson D, Sikora M, Kolb H. Pre- and postsynaptic mechanisms of spontaneous, excitatory postsynaptic currents in the salamander retina. Prog Brain Res 2001b;131:241–53.

Morgans CW. Presynaptic proteins of ribbon synapses in the retina. Microsc Res Technol 2000;50:141–50.

Moser T, Beutner D. Kinetics of exocytosis and endocytosis at the cochlear inner hair cell afferent synapse of the mouse. Proc Natl Acad Sci USA 2000;97:883–8.

Nachman-Clewner M, St Jules R, Townes-Anderson E. L-type calcium channels in the photoreceptor ribbon synapse: localization and role in plasticity. J Comp Neurol 1999;415:1–16.

Neves G, Lagnado L. The kinetics of exocytosis and endocytosis in the synaptic terminal of goldfish retinal bipolar cells. J Physiol 1999;515(Pt 1):181–202.

Palmer MJ, Hull C, Vigh J, von Gersdorff H. Synaptic cleft acidification and modulation of short-term depression by exocytosed protons in retinal bipolar cells. J Neurosci 2003;23:11332–41.

Partin KM, Fleck MW, Mayer ML. AMPA receptor flip/flop mutants affecting deactivation, desensitization, and modulation by cyclothiazide, aniracetam, and thiocyanate. J Neurosci 1996;16:6634–47.

Roberts WM. Localization of calcium signals by a mobile calcium buffer in frog saccular hair cells. J Neurosci 1994;14:3246–62.

Roberts WM, Jacobs RA, Hudspeth AJ. Colocalization of ion channels involved in frequency selectivity and synaptic transmission at presynaptic active zones of hair cells. J Neurosci 1990;10:3664–84.

Singer JH, Diamond JS. Sustained Ca^{2+} entry elicits transient postsynaptic currents at a retinal ribbon synapse. J Neurosci 2003;23:10923–33.

Singer JH, Lassova L, Vardi N, Diamond JS. Coordinated multivesicular release at a mammalian ribbon synapse. Nat Neurosci 2004;7:826–33.

Sjöstrand FS. The ultrastructure of the retinal rod synapses of the guinea pig eye. J Appl Phys 1953;24:1422.

Sjöstrand FS. Ultrastructure of retinal rod synapses of the guinea pig eye as revealed by three-dimensional reconstructions from serial sections. J Ultrastruct Res 1958;2:122–70.

Smith CA, Sjöstrand FS. Structure of the nerve endings on the external hair cells of the guinea pig cochlea as studied by serial sections. J Ultrastruct Res 1961;5:523–56.

Stevens CF, Wang Y. Facilitation and depression at single central synapses. Neuron 1995;14:795–802.

Stevens ER, Esguerra M, Kim PM, Newman EA, Snyder SH, Zahs KR, et al. D-Serine and serine racemase are present in the vertebrate retina and contribute to the physiological activation of NMDA receptors. Proc Natl Acad Sci USA 2003;100:6789–94.

Stiles JR, Bartol Jr TM. Monte Carlo methods for simulating realistic synaptic microphysiology using MCell. In: De Schutter E, editor. Computational neuroscience: realistic modeling for experimentalists. Boca Raton, FL: CRC Press; 2001. p. 87–127.

Stiles JR, Van HD, Bartol Jr TM, Salpeter EE, Salpeter MM. Miniature endplate current rise times less than 100 microseconds from improved dual recordings can be modeled with passive acetylcholine diffusion from a synaptic vesicle. Proc Natl Acad Sci USA 1996;93:5747–52.

Taylor WR, Chen E, Copenhagen DR. Characterization of spontaneous excitatory synaptic currents in salamander retinal ganglion cells. J Physiol 1995;486(Pt 1):207–21.

Thoreson WB. Dihydropyridine-sensitive calcium currents in bipolar cells of salamander retina are inhibited by reductions in extracellular chloride. Neurosci Lett 2000;280:155–8.

Thoreson WB, Rabl K, Townes-Anderson E, Heidelberger R. A highly Ca^{2+}-sensitive pool of vesicles contributes to linearity at the rod photoreceptor ribbon synapse. Neuron 2004;42:595–605.

Vollrath L, Huss H. The synaptic ribbons of the guinea-pig pineal gland under normal and experimental conditions 1. Z Zellforsch Mikrosk Anat 1973;139:417–29.

von Gersdorff H, Matthews G. Dynamics of synaptic vesicle fusion and membrane retrieval in synaptic terminals. Nature 1994;367:735–9.

von Gersdorff H, Matthews G. Depletion and replenishment of vesicle pools at a ribbon-type synaptic terminal. J Neurosci 1997;17:1919–27.

von Gersdorff H, Vardi E, Matthews G, Sterling P. Evidence that vesicles on the synaptic ribbon of retinal bipolar neurons can be rapidly released. Neuron 1996;16:1221–7.

Wachtel AW, Szamier RB. Special cutaneous receptor organs of fish: the tuberous organs of *Eigenmannia*. J Morphol 1966;119:51–80.

Wersall J, Flock A, Lundquist PG. Structural basis for directional sensitivity in cochlear and vestibular sensory receptors. Cold Spring Harb Symp Quant Biol 1965;30:115–32.

Zenisek D, Matthews G. The role of mitochondria in presynaptic calcium handling at a ribbon synapse. Neuron 2000;25:229–37.